



Harmonic Response Analysis of Seismic Excitations on Tunnel Linings



Pramod Sinha^{1*}, Masengo Ilunga², Tshering Tobgyel³

¹ Fixed Term Academic, University of South Africa, 1709 Pretoria, South Africa

² Department of Civil Engineering, University of South Africa, 1709 Pretoria, South Africa

³ Civil Engineering Department, CST, Royal University of Bhutan, 00975 Phuentsholing, Bhutan

* Correspondence: Pramod Sinha (sinha@mweb.co.za)

Received: 07-23-2023

Revised: 09-07-2023

Accepted: 09-15-2023

Citation: P. Sinha, M. Ilunga, and T. Tobgyel, "Harmonic response analysis of seismic excitations on tunnel linings," *GeoStruct. Innov.*, vol. 1, no. 1, pp. 1–16, 2023. <https://doi.org/10.56578/gsi010101>.



© 2023 by the author(s). Published by Acadlore Publishing Services Limited, Hong Kong. This article is available for free download and can be reused and cited, provided that the original published version is credited, under the CC BY 4.0 license.

Abstract: Tunnel linings, depending on their geographical locations, are exposed to various magnitudes of seismic loads. Ensuring that these linings resist seismic perturbations without exhibiting failures, such as crack initiation or propagation, is paramount. In the presented study, the structural stability of tunnel linings under pronounced seismic excitations was rigorously evaluated. Seismic excitations, in compliance with the IS 1893: 2002 code for both zone II and zone III conditions, were administered. Computer-Aided Design (CAD) modelling, static structural, and harmonic excitation analyses were meticulously conducted via the ANSYS finite element analysis (FEA) simulation package. From these comprehensive analyses, critical zones within the tunnel linings were identified under varying excitation frequencies. It was observed that, predominantly, these critical regions are situated at the corners of the tunnel linings, specifically in the bottom areas. Distinct maximum and minimum induced normal stresses within the tunnel structure were ascertained. Under a seismic excitation of .1g, a maximum reaction force of 1232.1 kN was derived. Conversely, for a seismic excitation of .16g, the reaction force peaked at a 1Hz frequency with a magnitude of 1971.3 kN. These findings furnish pivotal insights into the structural performance of tunnel linings when subjected to seismic disturbances, providing tunnel engineers and designers with invaluable knowledge to augment the resilience and safety of tunnel infrastructures.

Keywords: Tunnel linings; Seismic loads; Structural stability; Seismic excitation; ANSYS FEA; Critical zones; Normal stresses; Reaction force; Tunnel design

1 Introduction

With the escalating demand for subterranean habitats, significant advancements in tunnel design theory and construction practices have been observed. However, challenges, such as lining splits and segmental damages, continue to imperil structural integrity, especially when particular tunnel segments endure elevated bending moments from earth pressures and other extraneous stresses [1, 2]. Notably, such challenges have been found to correlate with tunnel geometric characteristics. Although an array of configurations has been utilized in tunnel engineering [3], circular tunnels are frequently selected, attributed to their construction simplicity and adaptability to practical layouts.

Tunnel construction, a multifaceted venture, necessitates a myriad of technical instruments and a proficient workforce consisting of adept technicians and engineers. A prevailing oversight among tunnel engineers appears to be the long-term interaction between rock rheological properties and tunnel linings. Such neglect has been linked to structural failures during tunnel operations [4–7]. Moreover, it has been identified that the primary tunnel lining undergoes degradation over time, subjected to extreme environmental conditions and its inherent structural attributes such as low density and high permeability. The tunnel's stability is largely governed by the interaction between its concrete lining and the surrounding granite. Given these findings, understanding these intricate delayed behavior is essential in tunnel longevity assessments.

Several scholars have developed various analytical methods to gauge the seismic forces exerted on tunnel linings. These methods, grounded in specific assumptions and contexts, have provided valuable insights, despite certain limitations [8]. Such analytical solutions, albeit simplified, offer a convenient approach, especially during

initial design phases. Concurrently, the realm of numerical analysis has seen advancements, especially in material deformation and stability modelling, facilitated by progressive strides in computational technology.

Present computational techniques, encompassing finite element, discrete element, and finite difference methods, are adopted extensively for the evaluation of subterranean structures [8]. Such methods have been made more feasible with technological advancements. Notably, three-dimensional models have been efficacious in discerning bending and axial deformations. In many computational models, the tunnel is spatially discretised, with the surrounding environment either similarly represented or symbolized through springs. Software applications like ABAQUS and FLAC have been harnessed to aid these analyses.

Tunnels, when exposed to seismic stresses, have been determined to undergo two principal deformation types [9]. The initial deformation appears torsional in nature, attributed to shear waves radiating perpendicular to the tunnel's longitudinal axis. Following this, tunnels exhibit axial compression and extension, caused by seismic wave components aligning with the tunnel's axis.

Extensive studies have explored shear deformations in tunnels, especially those due to vertically propagating shear waves [10, 11]. The importance of such deformation, especially under seismic pressures, has been emphasized consistently in literature. Interior tunnel surfaces, typically categorized as subterranean structures, have been found vulnerable to ground deformations, being often subjected to two-dimensional plane strain conditions.

To understand tunnel reactions to such shear deformations, two main methodologies have been predominantly employed. One involves the application of finite element techniques, focusing on dynamic and nonlinear evaluations between the soil and the tunnel structure.

Recent studies have shed light on pivotal factors governing tunnel stability and performance. A synthesis of these investigations accentuates the significance of diverse elements in comprehending and refining tunnel construction. In a notable study, the Monte Carlo approach was utilized by Do et al. [12] to examine the potential of tunnel collapses over its operational lifetime. In their analysis, two linings crafted from viscoelastic Burgers granite were taken into consideration, revealing insights into the structural tenacity inherent in tunnel systems.

Liu et al. [5] probed the intricate nexus between lining degradation and the mechanical behavior of tunnels situated in Generalized Kelvin rock. Their findings accentuated that pressures on lining structures predominantly emanate from the rheological attributes of the embedded rock. Over extended periods, such pressures intensify, culminating in conspicuous declines in tunnel longevity. Earlier studies have highlighted concrete modulus degradation in primary liners over their lifespan, leading to the inception of streamlined models delineating concrete lining deterioration, particularly spotlighting the gradual attenuation in primary lining rigidity.

In their categorization of numerical modelling techniques for double-arch tunnels, Lee et al. [13] distinguished between two methodologies: ground-structure and load-structure. The chosen method depended on the representation of the adjacent geological contexts. The ground-structure methodology, in particular, deployed finite element techniques to encapsulate both the surrounding granite and the linings. This necessitated meticulous evaluations of the elasto-plastic features of the granite and the elasticity inherent in concrete linings.

Ding et al. [14] postulated that pressures on tunnel spans, both half and full, could potentially mirror the relaxation pressures post the edification of a double-arch tunnel. Their research underscored the congruence between anticipated rock load dispersal and empirical measurements from terrestrial highway tunnels, accentuating the pragmatic ramifications of their research.

Experimental inquiries into tunnel linings were undertaken by Zhai et al. [15], revealing the profound ramifications of structural discontinuities at segment intersections, especially post the amalgamation of steel plates to buttress segmental tunnel linings. Such anomalies significantly influenced the distribution of inter-facial stresses and the progression of de-bonding. Furthermore, the inherent subterranean nature of tunnels introduced intricacies in soil-structure interactions, as tunnels grappled with augmented resistance from the ambient soil during deformation.

Collectively, these cornerstone studies enrich the current comprehension of the multifaceted dynamics in tunnel engineering, elucidating determinants influencing tunnel stability, resilience, and extended performance.

However, notwithstanding these advances in tunnel engineering, discernible lacunae persist, especially concerning deformation effects on reinforcing steel plates. In the context of tunnel rehabilitation, understanding the ramifications of such deformations holds paramount significance. A pressing research query emerges: How might the findings from such investigations refine rehabilitation duration predictions for tunnels subjected to deformations?

The structural integrity of tunnel linings, particularly when confronted with high-magnitude seismic excitations, remains a salient concern. This study endeavors to elucidate this issue by rigorously assessing the structural robustness of tunnel linings under seismic disturbances, aligned with the stipulations of the IS 1893: 2002 code, encapsulating both Zone II and Zone III criteria. Through an exhaustive assessment, complemented by CAD modelling and ANSYS FEA simulations, an enhanced understanding of tunnel lining behavior under seismic afflictions is anticipated. Such findings promise to not only deepen current knowledge but also to foster accurate rehabilitation duration predictions, contributing to a safer and robust tunnel infrastructure.

2 Methodology

In the present research, a meticulous FEA of the tunnel was undertaken using the ANSYS simulation package. Seismic analysis was performed in compliance with the IS 1893: 2002 code, drawing data from the extant seismic hazard map of India (as elucidated in Figure 1) [16].

The computational domain for the tunnel, as delineated within ANSYS Design Modeler, encompasses a breadth of 150m by 150m, with dimensions sourced from pertinent academic literature [17]. A visual representation of the tunnel and its computational domain is provided in Figure 2.

Subjected to a confluence of topographical and traffic burdens, the tunnel lining structure mandated intricate structural boundary conditions. These conditions encompassed both vehicular and geotechnical ramifications, as demonstrated in Figure 3.

In congruence with the Austrian tunneling guideline RVS 09.01.23, aerodynamic effects resultant from traffic were integrated. A pressure of 1.5 kN/m² was ascribed, attributing it to traffic-induced burdens. The subsequent phase of analysis incorporated seismic loads, post the elucidation of static structural burdens.

Seismic hazard evaluations, specifically centring on Peak Ground Acceleration (PGA) in relation to Maximum Considered Earthquake (MCE) ground motion, were drawn from the zonal demarcations present in India's seismic hazard map (refer to Figure 1). For regions like the Koyna area, known for a mean return period of 2500 years for the Maximum Considered Earthquake, the anticipated maximum ground motion oscillates between 0.34 and 0.6 g.

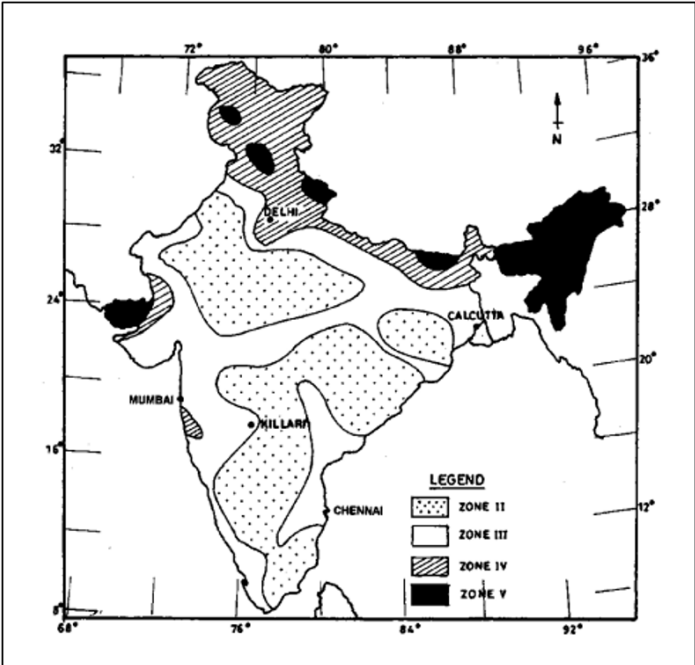


Figure 1. Seismic zoning map of India [16]

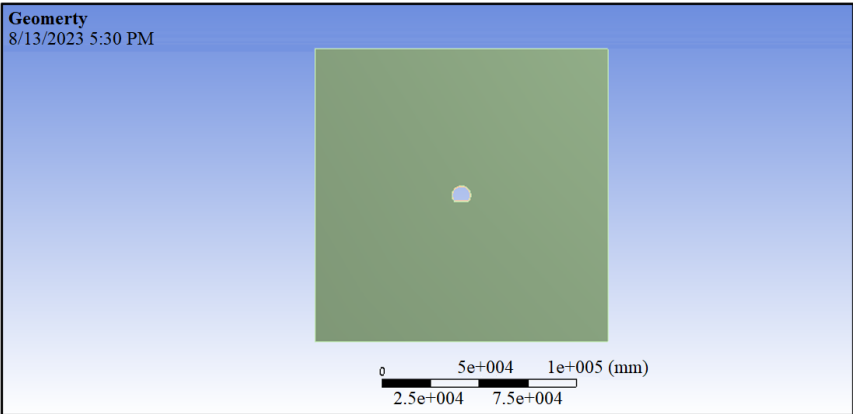


Figure 2. CAD model of computational domain

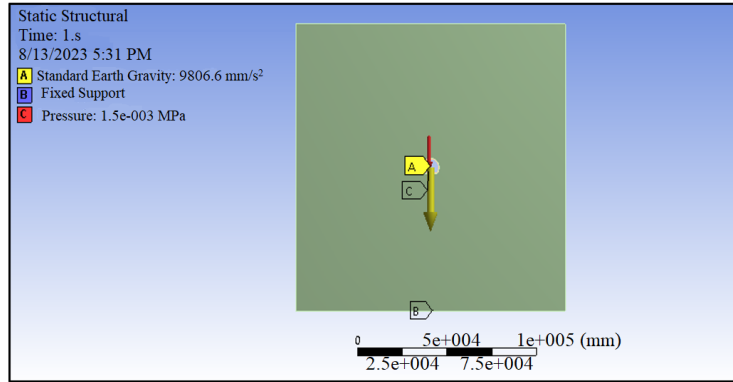


Figure 3. Structural loads on computational domain

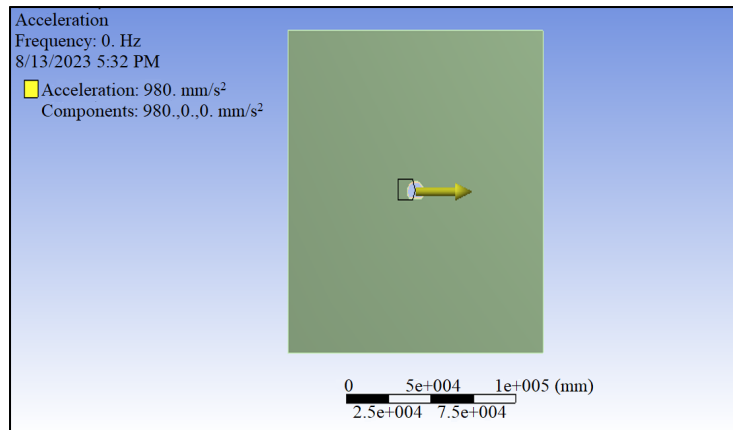


Figure 4. Seismic excitation of .1 g applied on the computational domain

Frequency Spacing	Linear
<input type="checkbox"/> Range Minimum	0. Hz
<input type="checkbox"/> Range Maximum	10. Hz
<input type="checkbox"/> Solution Intervals	10
User Defined Frequencies	Off
Solution Method	Mode Superposition
Include Residual Vector	No
Cluster Results	No
Modal Frequency Range	Program Controlled
Store Results At All Frequencies	Yes

Figure 5. Seismic excitation of .1 g applied on the computational domain

Seismic burdens administered to the structure were discerned from zones II and III, each epitomising distinct seismic excitation intensities. Zone II, delineating a region of minimal seismic risk, encompasses territories such as North India, inclusive of states like Delhi, Punjab, among others. Seismic excitations in this demarcation were observed to be of magnitude PGA 0.1 g. Conversely, Zone III, emblematic of moderate seismic risk, spans significant swathes of North and Western India. Here, the PGA is pegged at 0.16 g, recording a heightened seismic activity compared to Zone II. The seismic exertion, applied laterally as illustrated in Figure 4, was supplemented by harmonic excitation frequencies spanning 0 Hz to 10 Hz, as inferred from seismic datasets [17]. A visual delineation of these seismic frequencies' application is proffered in Figure 5.

Upon the imposition of seismic excitations, simulations were executed encompassing matrix formulation, inversion, and multiplication. Through this approach, profound insights into the seismic behavioral dynamics

of the tunnel were garnered.

3 Results and Discussion

Insights derived from the FEA encapsulate both static structural and harmonic analyses, elucidating the behavioral nuances of the tunnel structure under multifarious conditions. Deformation from the FEA analysis is presented in Figure 6, revealing a peak deformation of 335 mm, a value resonating closely with extant literature findings [17].

In-depth scrutiny via FEA simulation for static structural analysis was performed across a spectrum of seismic excitation frequencies, delineated in Figure 7 through Figure 20.

When subjected to a frequency of 1 Hz, the zenith of deformation was detected at the apex of the computational domain, reaching a magnitude of 43 mm. Within the tunnel lining, deformation peaked at 20.168 mm.

Elevating the frequency to 2 Hz, the deformation's pinnacle at the computational domain's apex scaled down to 9.52 mm, while the tunnel lining evidenced a deformation of 4.4046 mm.

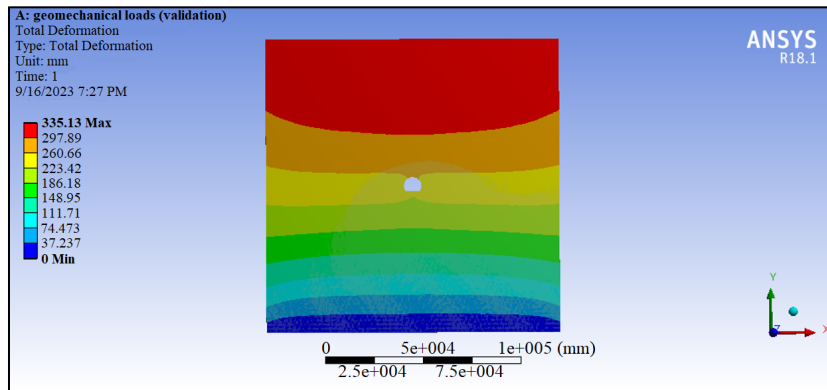


Figure 6. Deformation plot on tunnel structure

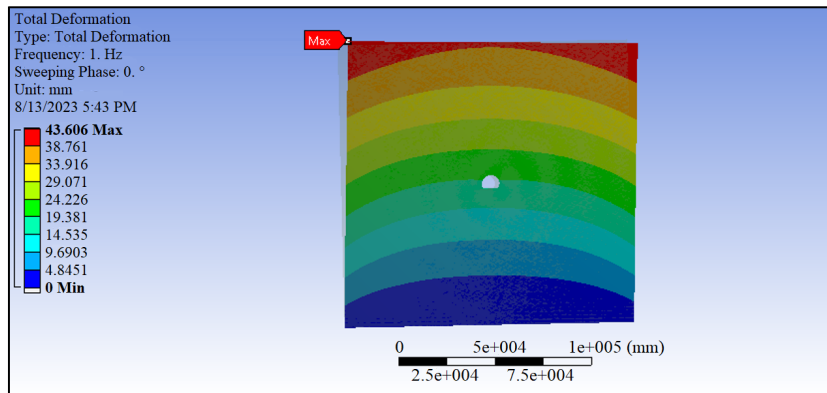


Figure 7. Deformation plot at 1 Hz seismic excitation

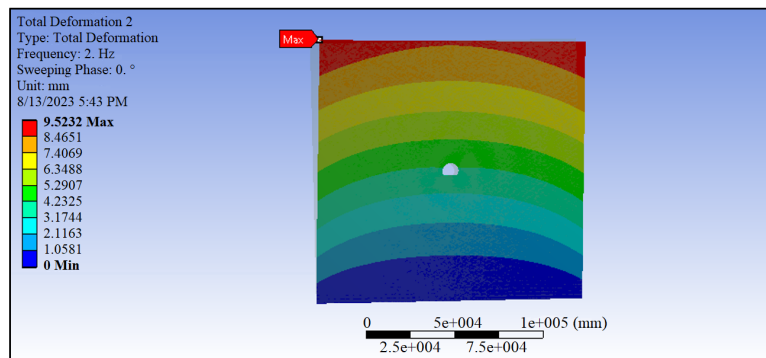


Figure 8. Deformation plot at 2 Hz seismic excitation

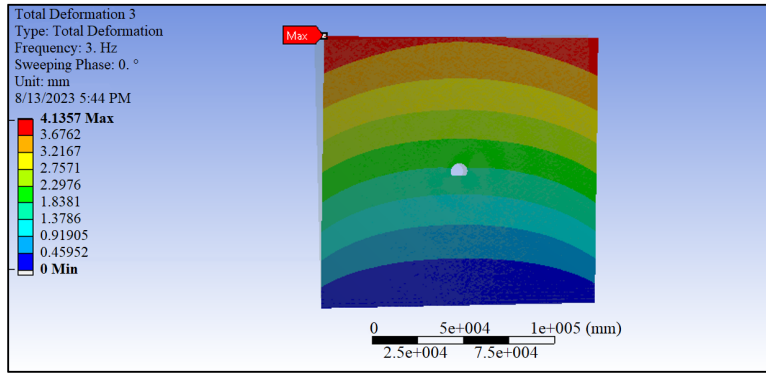


Figure 9. Deformation plot at 3 Hz seismic excitation

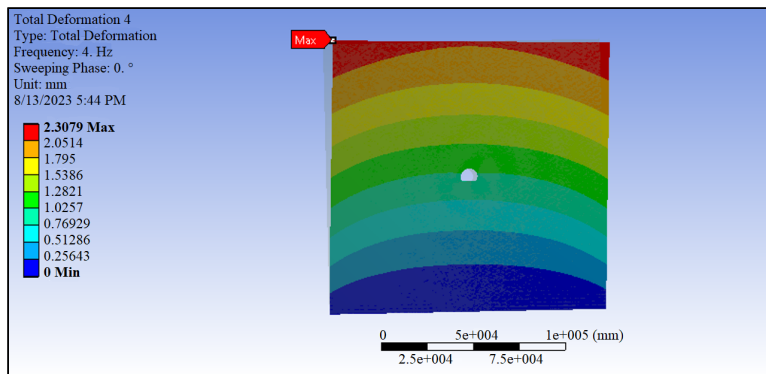


Figure 10. Deformation plot at 4 Hz seismic excitation

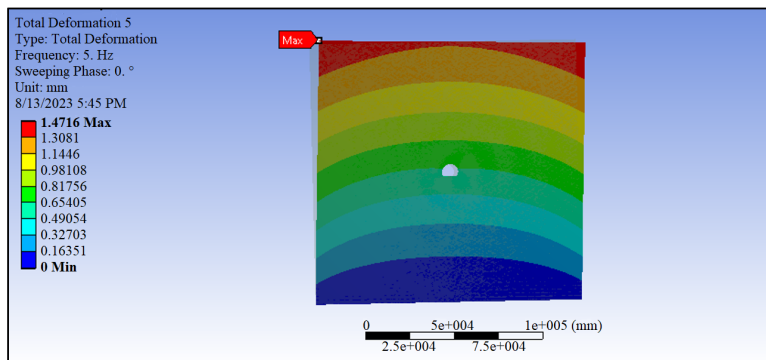


Figure 11. Deformation plot at 5 Hz seismic excitation

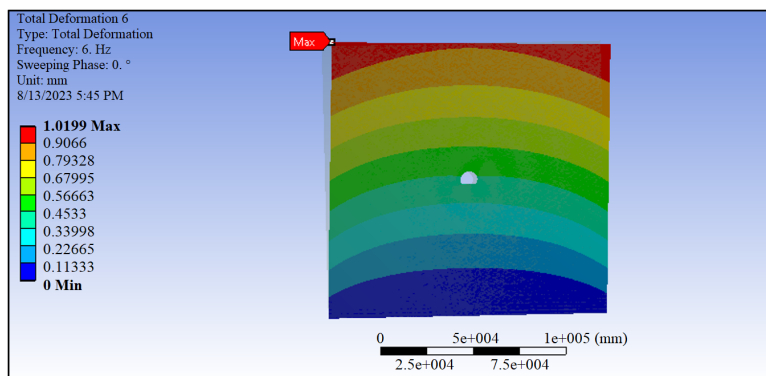


Figure 12. Deformation plot at 6 Hz seismic excitation

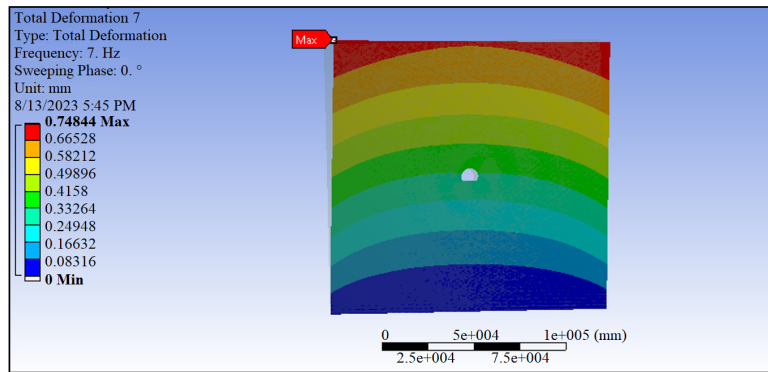


Figure 13. Deformation plot at 7 Hz seismic excitation

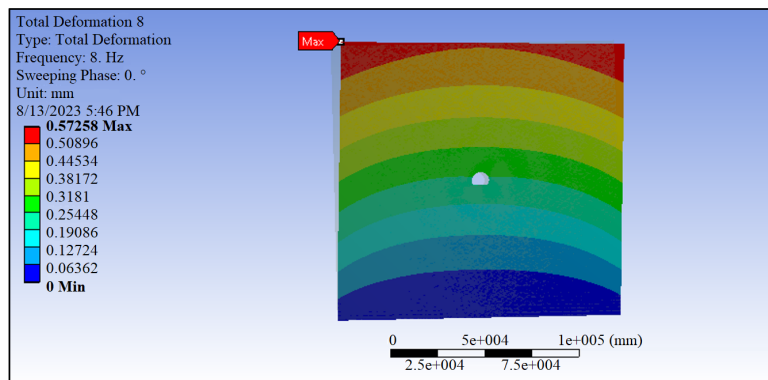


Figure 14. Deformation plot at 8 Hz seismic excitation

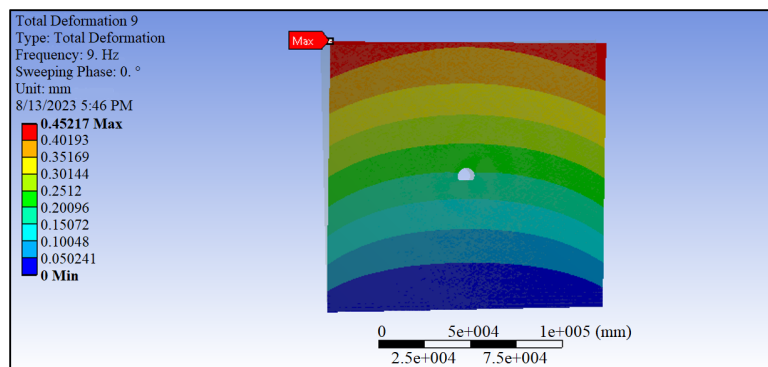


Figure 15. Deformation plot at 9 Hz seismic excitation

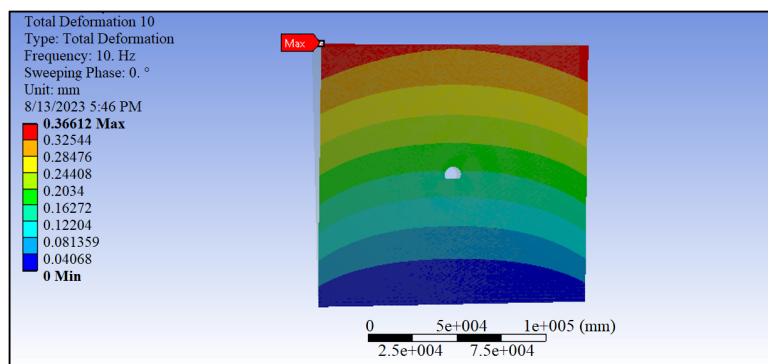


Figure 16. Deformation plot at 10 Hz seismic excitation

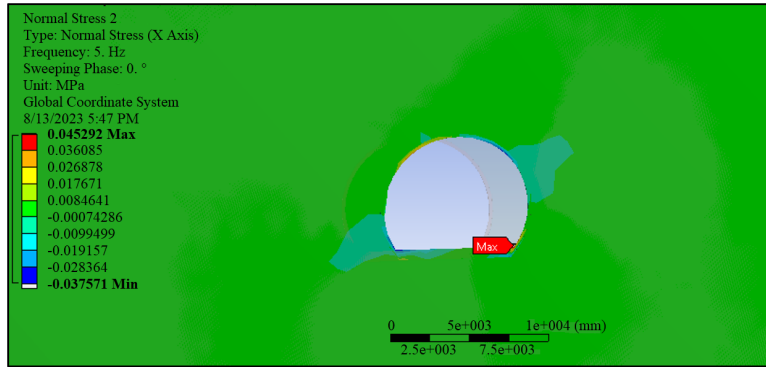


Figure 17. Normal stress plot at 5 Hz seismic excitation

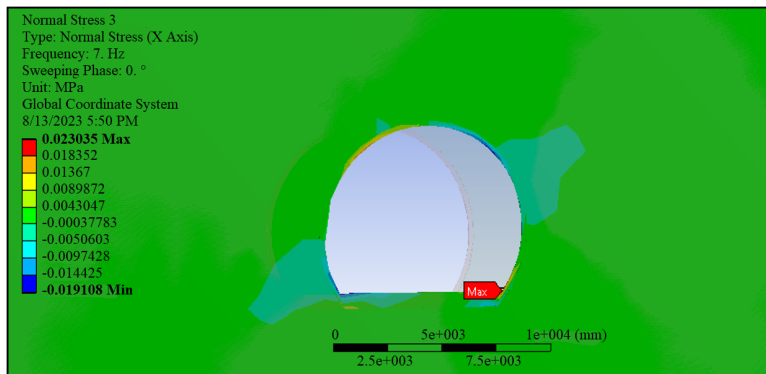


Figure 18. Normal stress plot at 7 Hz seismic excitation

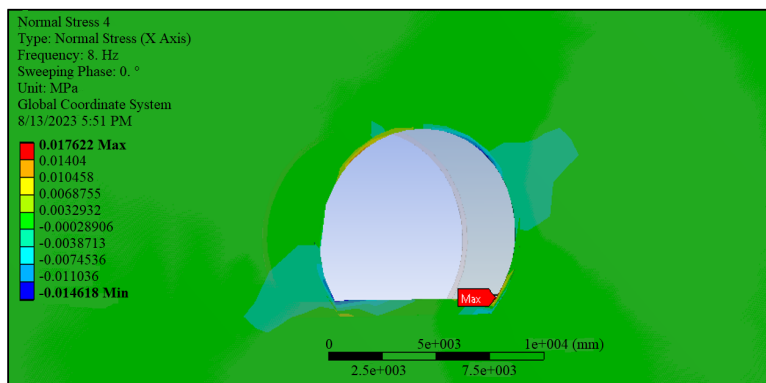


Figure 19. Normal stress plot at 8 Hz seismic excitation

At a seismic excitation of 3 Hz, deformation peaking at 4.135 mm was identified at the apex of the computational domain. Concurrently, the tunnel lining evidenced a pronounced deformation, reaching an amplitude of 1.9128 mm.

When the seismic frequency was augmented to 4 Hz, a salient deformation of 2.3079 mm was observed at the computational domain's zenith. The tunnel lining, in tandem, manifested a deformation with a magnitude of 1.0674 mm.

Exposure to a 5 Hz seismic frequency induced a deformation apex of 1.4716 mm within the computational domain. Simultaneously, a consistent deformation magnitude of 1.0674 mm was recorded within the tunnel lining.

As the seismic excitation was increased further to 6 Hz, the computational domain's apex registered a deformation of 1.0199 mm, while a deformation of 0.47173 mm was ascertained within the tunnel lining.

Lastly, at a seismic excitation of 7 Hz, the computational domain's pinnacle deformation was recorded as 0.748 mm, and the tunnel lining depicted a deformation peaking at 0.3461 mm.

Further analysis revealed that at an 8 Hz seismic frequency, a deformation of 0.572 mm was identified at the pinnacle of the computational domain. Meanwhile, within the tunnel lining, a deformation peak of 0.26482 mm was detected.

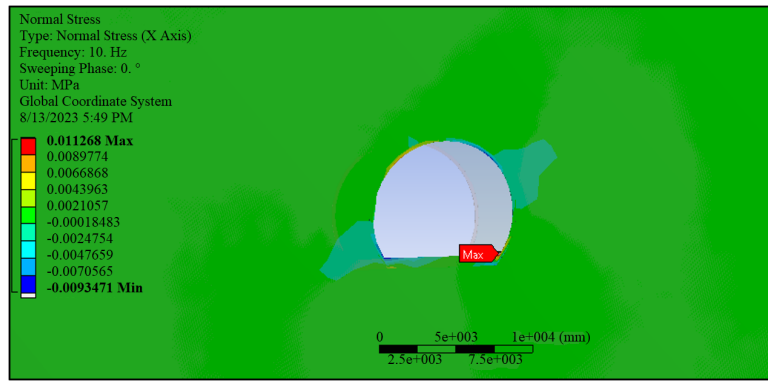


Figure 20. Normal stress plot at 10 Hz seismic excitation

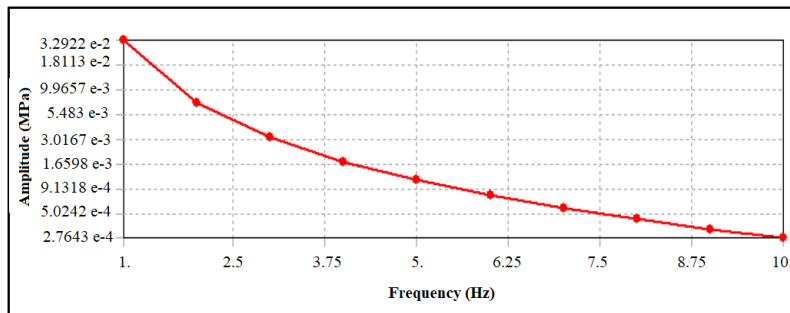


Figure 21. Frequency response of horizontal normal stress at .1 g seismic excitation

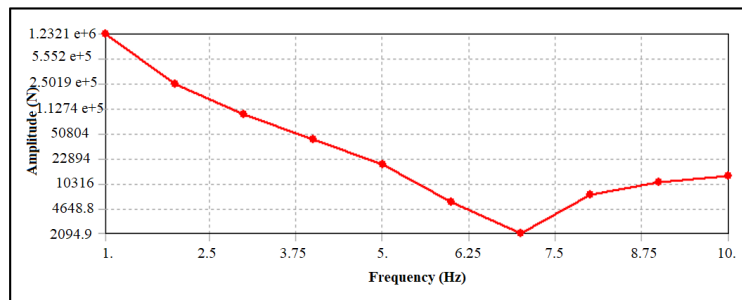


Figure 22. Frequency response of horizontal force at .1 g seismic excitation

Subsequently, a 9 Hz seismic excitation manifested a peak deformation of 0.452 mm at the computational domain's apex, and the tunnel lining exhibited a significant deformation, measuring 0.20913 mm.

Ultimately, when the system was subjected to a 10 Hz seismic frequency, the computational domain highlighted a maximum deformation of 0.366mm. In tandem, the tunnel lining was found to display a deformation reaching a magnitude of 0.169 mm.

An essential facet of the conducted analysis pertained to the distribution of normal stress within the computational domain, as depicted in Figure 17 through Figure 20. Within this domain, compressive behavior was denoted by negative values in the normal stress. Notably, the peak compressive stress was documented to be 0.037 MPa, whereas the tunnel lining presented a maximum tensile stress of 0.0452 MPa.

At the domain's corner, a negative normal stress was observed, indicative of compressive behaviour. From the assessment, a compressive stress peak of 0.091 MPa was documented, while the tunnel lining manifested a tensile stress, reaching a magnitude of 0.02303 MPa, as depicted in Figure 18.

Similarly, an analysis corresponding to another set of parameters revealed a maximum compressive stress of 0.0146 MPa. Concurrently, the tunnel lining demonstrated a tensile stress peaking at 0.0176 MPa, as illustrated in Figure 19.

Further examination, showcased in Figure 20, identified a compressive stress pinnacle of 0.0093 MPa. In parallel, a tensile stress of 0.0112 MPa was noted within the tunnel lining.

Data pertaining to the relationship between horizontal normal stress and frequency was derived from the analysis,

as depicted in Figure 21. It was observed that the highest induced normal stress occurred at a lower frequency of 1 Hz and demonstrated a non-linear decrease with the escalation in excitation frequency. The least induced stress was discerned at a frequency of 10 Hz.

Figure 22 portrays the variation in reaction force in relation to the frequency shift. A decline in horizontal reaction force was noted as the natural frequency increased. The most pronounced reaction force, as extrapolated from the analysis, stood at 1232.1 kN. The least reaction force, measured at 2.0949 kN, was detected at an 8 Hz frequency, whereas an excitation of 10 Hz resulted in a horizontal force of 13.1 kN.

Upon subjecting the structure to a seismic excitation of 0.16 PGA, deformation plots were procured for various frequencies, as showcased in Figure 23. At a seismic excitation of 1 Hz, a peak deformation of 32.26 mm was documented at the tunnel lining. In contrast, a 2 Hz seismic excitation yielded a maximum deformation of 7.0473 mm at the tunnel lining, further elucidated in Figure 24.

From the deformation plot obtained at 3 Hz seismic excitation, the maximum deformation obtained at tunnel lining is 3.0605 mm as shown in Figure 25.

From the deformation plot obtained at 4 Hz seismic excitation, the maximum deformation obtained at tunnel lining is 1.7079 mm as shown in Figure 26.

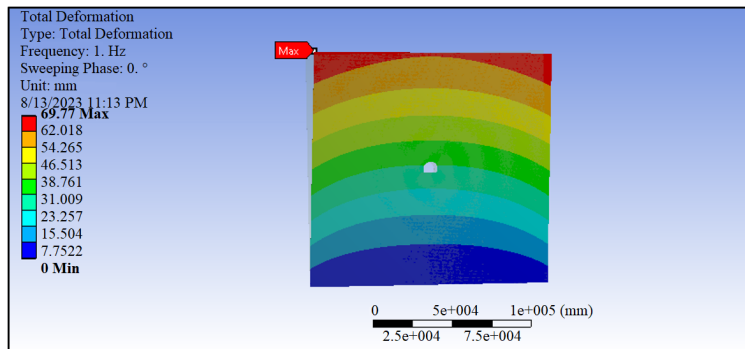


Figure 23. Deformation plot at 1 Hz seismic excitation for .16 g seismic excitation

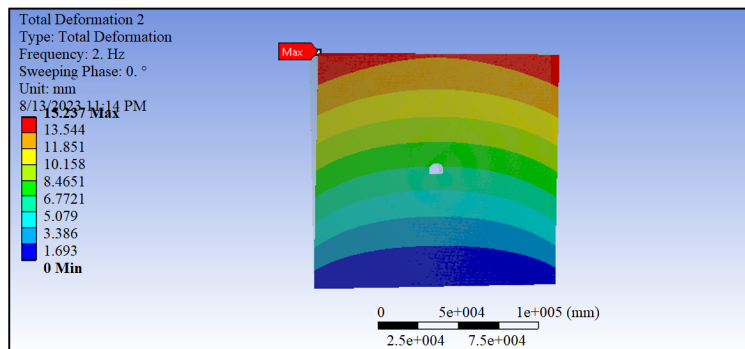


Figure 24. Deformation plot at 2 Hz seismic excitation for .16 g seismic excitation

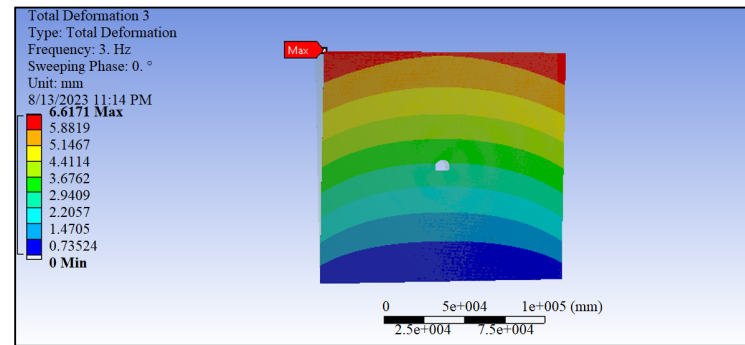


Figure 25. Deformation plot at 3 Hz seismic excitation for .16 g seismic excitation

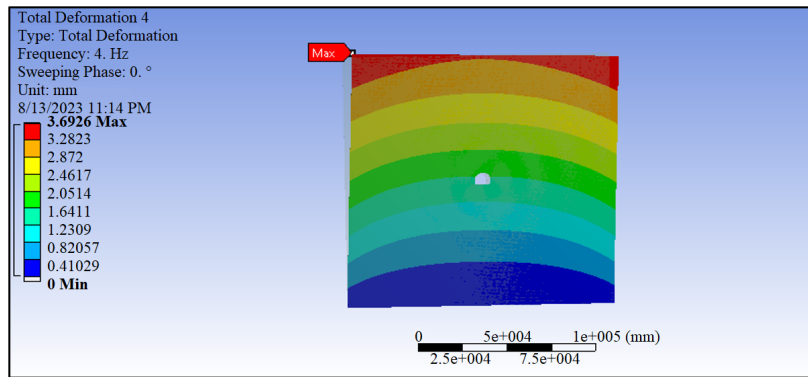


Figure 26. Deformation plot at 4 Hz seismic excitation for .16 g seismic excitation

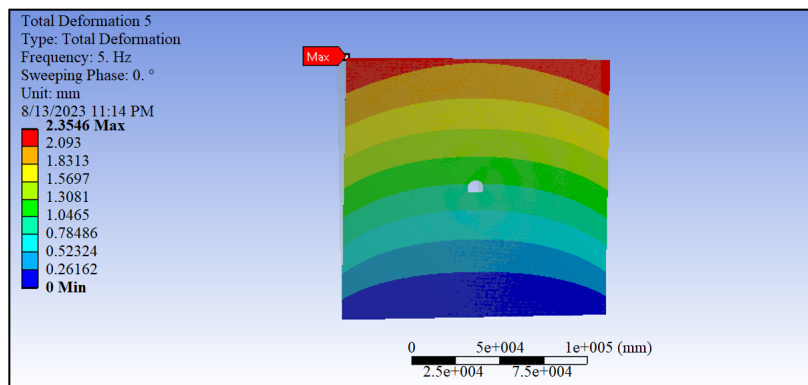


Figure 27. Deformation plot at 5 Hz seismic excitation for .16 g seismic excitation

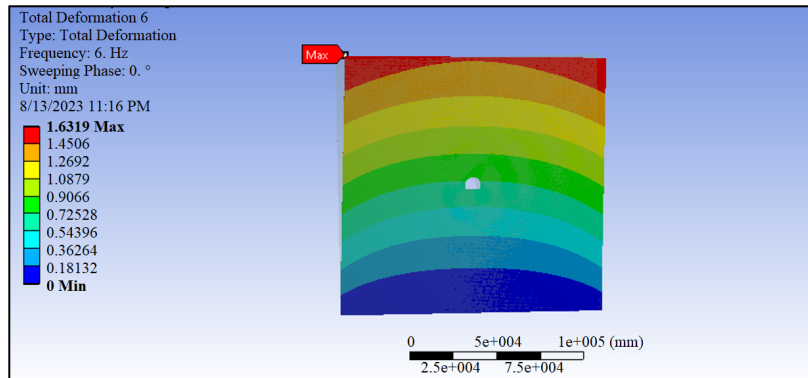


Figure 28. Deformation plot at 6 Hz seismic excitation for .16 g seismic excitation

From the deformation plot obtained at 5 Hz seismic excitation, the maximum deformation obtained at tunnel lining is 1.089 mm as shown in Figure 27.

From the deformation plot obtained at 6 Hz seismic excitation, the maximum deformation obtained at tunnel lining is .754 mm as shown in Figure 28.

From the deformation plot obtained at 7 Hz seismic excitation, the maximum deformation obtained at tunnel lining is .5538 mm as shown in Figure 29.

From the deformation plot obtained at 8 Hz seismic excitation, the maximum deformation obtained at tunnel lining is .4237 mm as shown in Figure 30.

From the deformation plot obtained at 9 Hz seismic excitation, the maximum deformation obtained at tunnel lining is .3346 mm as shown in Figure 31.

From the deformation plot obtained at 10Hz seismic excitation, the maximum deformation obtained at tunnel lining is .2709 mm as shown in Figure 32.

The normal stress distribution plot is obtained for tunnel wall lining at 5 Hz seismic excitation as shown in

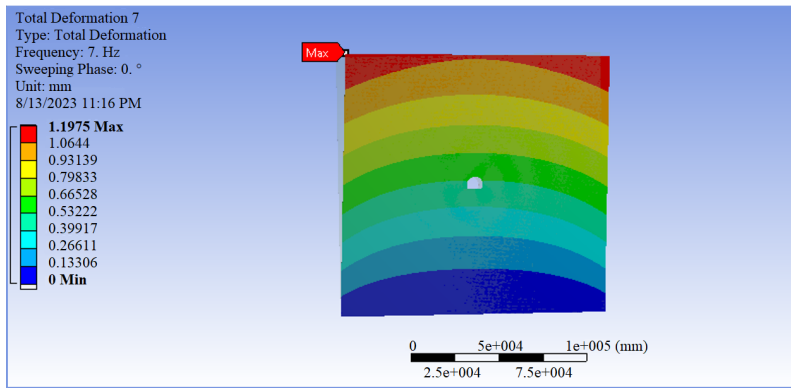


Figure 29. Deformation plot at 7 Hz seismic excitation for .16 g seismic excitation

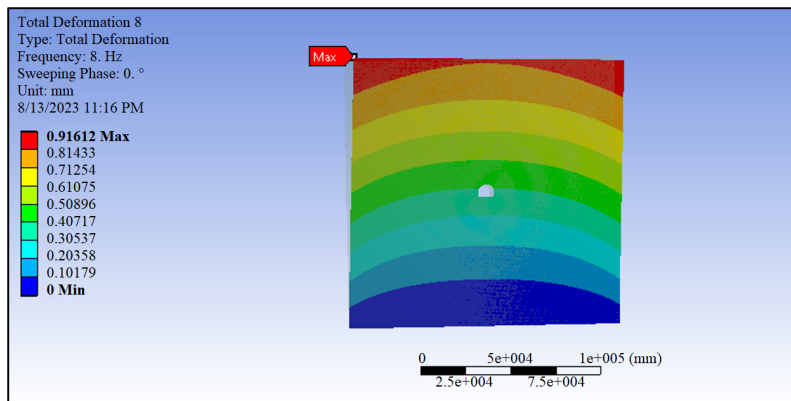


Figure 30. Deformation plot at 8 Hz seismic excitation for .16 g seismic excitation

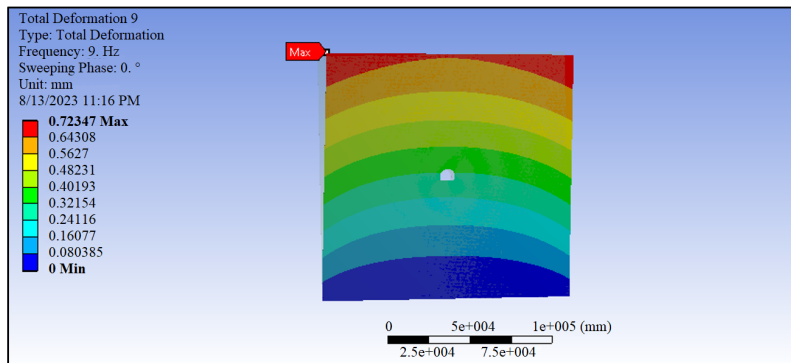


Figure 31. Deformation plot at 9 Hz seismic excitation for .16 g seismic excitation

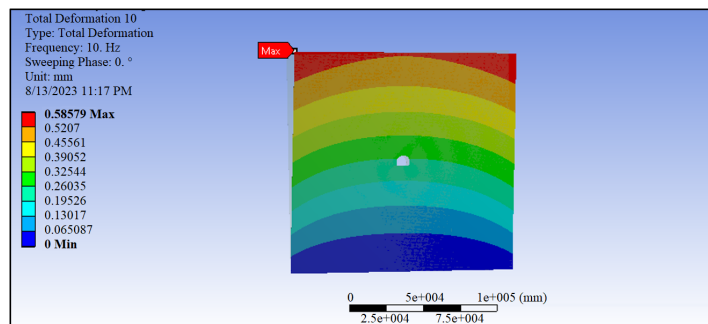


Figure 32. Deformation plot at 10 Hz seismic excitation for .16 g seismic excitation

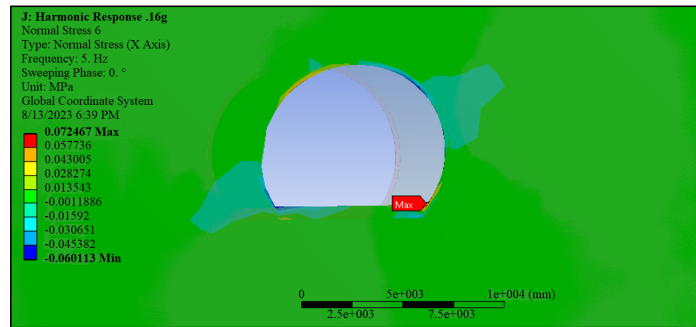


Figure 33. Normal stress plot at 5 Hz seismic excitation

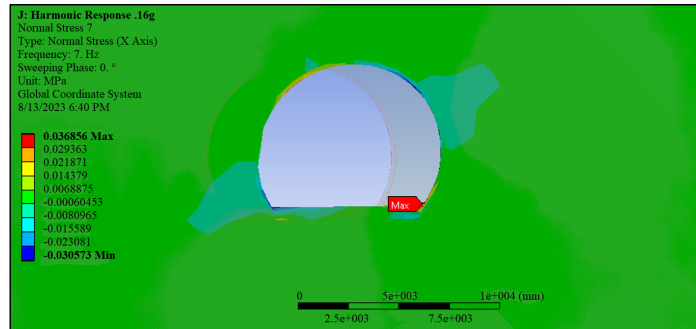


Figure 34. Normal stress plot at 7 Hz seismic excitation

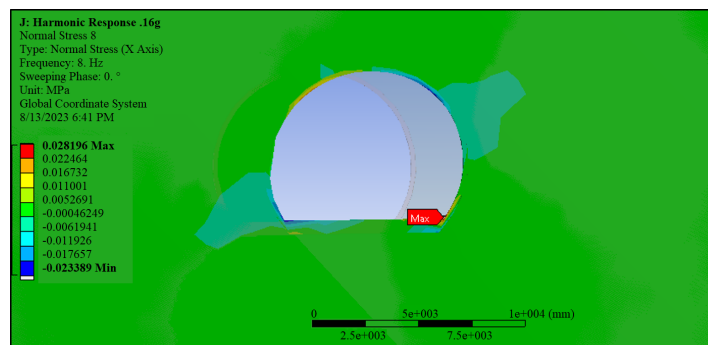


Figure 35. Normal stress plot at 8 Hz seismic excitation

Figure 33. The induced normal stress is uniform in most of the zones in the computational domain. The normal stress is tensile at the right corner and compressive at the left corner. The maximum tensile stress obtained is .072 MPa and maximum compressive stress is .0601 MPa.

At 7Hz frequency, the normal stress is tensile at the right corner and compressive at the left corner. The maximum tensile stress obtained is .036 MPa and maximum compressive stress is .0305 MPa as shown in Figure 34.

At a seismic excitation of 8 Hz, tensile normal stress was observed in the right corner region, whereas the left corner exhibited compressive stress. The highest tensile stress was recorded at 0.028 MPa, while the peak compressive stress reached 0.023 MPa, as depicted in Figure 35.

Upon increasing the seismic frequency to 9 Hz, similar stress behaviour was discerned, with tensile stresses manifesting in the right corner and compressive stresses in the left. In this instance, the maximal tensile and compressive stresses were determined to be 0.018 MPa and 0.014 MPa respectively, as illustrated in Figure 36.

Figure 37 elucidates the exponential decline of horizontal normal stress in relation to escalating excitation frequency. Notably, a frequency of 1 Hz induced a normal stress of 0.0526 MPa, which diminished to its nadir at 10 Hz, registering a mere 0.00044 MPa.

The relationship between horizontal reaction force and frequency variation is further delineated in Figure 38. It was observed that the reaction force decreased linearly with the intensification of excitation frequency up to 7 Hz, only to rise subsequently. The zenith of reaction force was recorded at a frequency of 1 Hz, measuring 1971.3 kN, whereas the nadir, a modest 3.35 kN, starkly contrasted the force of 20.9 kN witnessed at a 10Hz excitation. Such

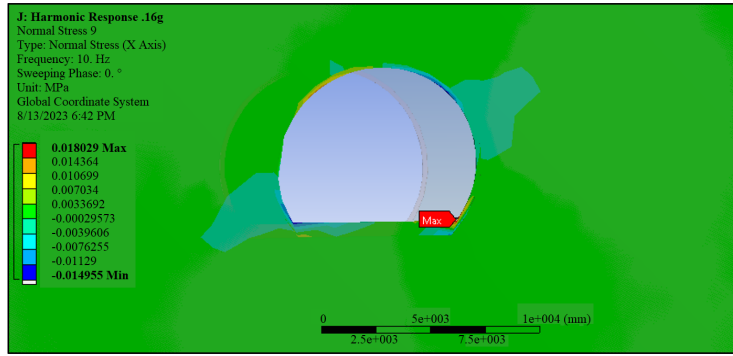


Figure 36. Normal stress plot at 9 Hz seismic excitation

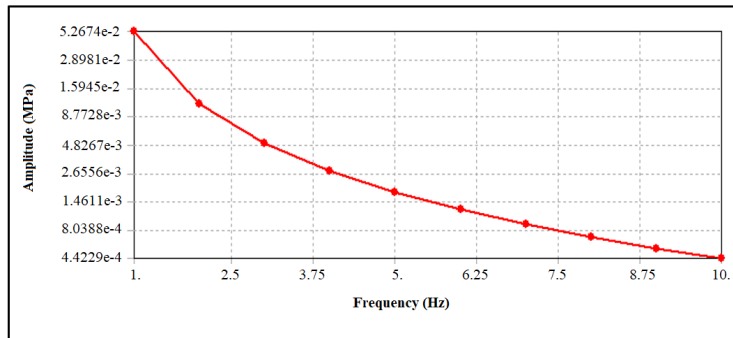


Figure 37. Frequency response of horizontal normal stress at .16 g amplitude

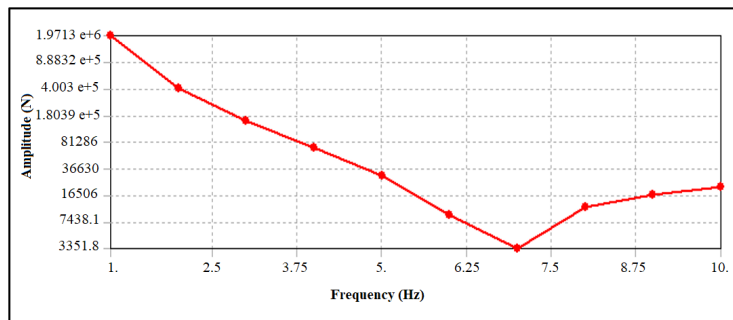


Figure 38. Frequency response of horizontal force reaction at .16 g amplitude

findings provide pivotal insights into the dynamic nuances of tunnel structures when subjected to seismic forces, serving as an invaluable compass for subsequent research endeavor in tunnel engineering and rehabilitation.

4 Conclusion

In the conducted study, a detailed seismic analysis was performed on tunnel structures under various excitations, particularly for magnitudes of 0.1 g and 0.16 g, encompassing both zone II and zone III seismic conditions. Through this examination, critical regions within the tunnel lining were identified, pinpointing areas particularly vulnerable to seismic-induced stresses. Notably, consistent observations were made that emphasize the bottom corners of the tunnel lining as zones of heightened sensitivity across an array of excitation frequencies. Assessment of induced normal stresses within the tunnel structure proved integral to this investigation. Under a seismic excitation of 0.1 g, a peak reaction force of 1232.1 kN was registered. However, for a 0.16 g seismic excitation, the most pronounced reaction force was recorded at 1 Hz, equating to 1971.3 kN. This investigation lays the groundwork for refining tunnel design methodologies and harnessing FEA to pinpoint areas within tunnel structures that are seismically critical. Furthermore, the marked differences in normal stress and deformation between tunnel structures situated in zones 2 and 3 underscore the pivotal role of regional seismic determinants in tunnel engineering. The knowledge procured from this study pertaining to seismic-induced stresses and their distribution can serve as a foundation for future explorations in this domain. The data presented herein is paramount for appraising critical regions and

understanding the ramifications of seismic excitation on tunnel structures. Prospective studies can harness these insights to better predict the duration required for rehabilitating tunnels that have undergone deformation. Moreover, subsequent research endeavor might venture deeper into analyzing the behaviour of reinforcing steel plates embedded within tunnel linings. The results presented have vast practical implications, ranging from enhancing tunnel designs to determining regions more prone to seismic activity. Those in the realm of engineering and tunnel design are poised to benefit immensely from these revelations, furthering the advancement of safer and more resilient tunnel infrastructures. Despite its contributions, this study is not devoid of limitations. Its scope was predominantly confined to discerning critical regions and evaluating the stresses they undergo during seismic events, without delving into the potential ramifications on the reinforcing steel plates of tunnel linings. While invaluable, the insights garnered warrant further research and validation prior to their practical application. In summation, this research offers a pivotal addition to tunnel engineering literature by unveiling nuanced seismic considerations and accentuating the significance of regional seismic risk variations. Such insights are integral to bolstering tunnel structures, ensuring they stand resilient against seismic threats. As the field evolves, it is anticipated that this work will act as a precursor to innovations in tunnel design and remediation techniques.

Data Availability

Not applicable.

Conflicts of Interest

The authors declare that they have no conflicts of interest.

References

- [1] Y. J. Zhao, S. Xing, Q. S. Zhang, F. S. Zhang, and W. Q. Ma, "Causes of maize density loss in farmers' fields in Northeast China," *J. Integr. Agric.*, vol. 18, no. 8, pp. 1680–1689, 2019. [https://doi.org/10.1016/S2095-3119\(18\)62101-X](https://doi.org/10.1016/S2095-3119(18)62101-X)
- [2] Y. Liu, C. Tang, P. Wang, Y. Guan, and S. Wang, "Study on disease mechanism and theoretical quantification method of tunnel structure," *Adv. Civ. Eng.*, vol. 2019, pp. 1–14, 2019. <https://doi.org/10.1155/2019/4398524>
- [3] W. Wu, "Tunnelling and tunnel mechanics-a rational approach to tunnelling by Dimitrios Kolymbas," *Acta Geotech*, vol. 1, no. 1, pp. 75–76, 2006. <https://doi.org/10.1007/s11440-006-0007-7>
- [4] Q. Ai, Y. Yuan, S. L. Shen, H. Wang, and X. Huang, "Investigation on inspection scheduling for the maintenance of tunnel with different degradation modes," *Tunn. Undergr. Sp. Tech.*, vol. 106, p. 103589, 2020. <https://doi.org/10.1016/j.tust.2020.103589>
- [5] C. Liu, D. Zhang, Q. Fang, S. Zhang, and Z. Sun, "Investigation of progressive failure mechanism of tunnel lining with material defects using discrete element method," *Theor. Appl. Fract. Mec.*, vol. 125, p. 103832, 2023. <https://doi.org/10.1016/j.tafmec.2023.103832>
- [6] A. Showkati, H. Salari-rad, and M. Hazrati Aghchai, "Predicting long-term stability of tunnels considering rock mass weathering and deterioration of primary support," *Tunn. Undergr. Sp. Tech.*, vol. 107, p. 103670, 2021. <https://doi.org/10.1016/j.tust.2020.103670>
- [7] F. Ye, N. Qin, X. Liang, A. Ouyang, Z. Qin, and E. Su, "Analyses of the defects in highway tunnels in china," *Tunn. Undergr. Sp. Tech.*, vol. 107, p. 103658, 2021. <https://doi.org/10.1016/j.tust.2020.103658>
- [8] Y. M. A. Hashash, J. J. Hook, B. Schmidt, and J. I. C. Yao, "Seismic design and analysis of underground structures," *Tunn. Undergr. Sp. Tech.*, vol. 16, no. 4, pp. 247–293, 2001. [https://doi.org/10.1016/S0886-7798\(01\)00051-7](https://doi.org/10.1016/S0886-7798(01)00051-7)
- [9] J. N. Wang and G. A. Munfakh, *Seismic Design of Tunnels*. WIT Press, 2001.
- [10] A. Amorosi and D. Boldini, "Numerical modelling of the transverse dynamic behaviour of circular tunnels in clayey soils," *Soil. Dyn. Earthq. Eng.*, vol. 29, no. 6, pp. 1059–1072, 2009. <https://doi.org/10.1016/j.soildyn.2008.12.004>
- [11] A. Bobet, "Effect of pore water pressure on tunnel support during static and seismic loading," *Tunn. Undergr. Sp. Tech.*, vol. 18, no. 4, pp. 377–393, 2003. [https://doi.org/10.1016/S0886-7798\(03\)00008-7](https://doi.org/10.1016/S0886-7798(03)00008-7)
- [12] D. P. Do, M. N. Vu, N. T. Tran, and G. Armand, "Closed-form solution and reliability analysis of deep tunnel supported by a concrete liner and a covered compressible layer within the viscoelastic burger rock," *Rock Mech. Rock Eng.*, vol. 54, no. 5, pp. 2311–2334, 2021. <https://doi.org/10.1007/s00603-021-02401-6>
- [13] J. K. Lee, H. Yoo, H. Ban, and W. J. Park, "Estimation of rock load of multi-arch tunnel with cracks using stress variable method," *Appl. Sci.*, vol. 10, no. 9, p. 3285, 2020. <https://doi.org/10.3390/app10093285>
- [14] W. Q. Ding, X. X. Wang, H. H. Zhu, L. D. Yang, and Z. H. Li, "Defining method for designing load of multi-arch tunnel," *China J. Highw. Transp.*, vol. 20, no. 5, pp. 78–82, 2007. <http://zgglxb.chd.edu.cn/EN/Y2007/V20/I5/78>

- [15] W. Zhai, D. Chapman, A. Faramarzi, H. Huang, and D. Zhang, "Multi-objective optimisation design for composite tunnel linings using non-dominated sorting genetic algorithm," *Geotech. Asp. Undergr. Constr. Soft Ground*, pp. 444–550, 2021.
- [16] "Indian standard criteria for earthquake resistant design of structures (fifth revision)," IS: 1893 (Part-1), Tech. Rep., 2002.
- [17] V. Agrahari, A. Chandramauli, and V. Balmiki, "Structural analysis of tunnel using fea," *Int. J. Glob. Acad. Sci. Res.*, vol. 2, no. 2, pp. 44–55, 2023. <https://doi.org/10.55938/ijgasr.v2i2.47>